

Communication

# Combined X-ray and Neutron Powder Diffraction Study on *B*-Site Cation Ordering in Complex Perovskite $\text{La}_2(\text{Al}_{1/2}\text{MgTa}_{1/2})\text{O}_6$

Yoo Jung Sohn <sup>1,\*</sup> , Volodymyr Baran <sup>2,3</sup>, Ralph Gilles <sup>2</sup> , Georg Roth <sup>4</sup> and Robert Vaßen <sup>1</sup> 

<sup>1</sup> Institute of Energy and Climate Research, Materials Synthesis and Processing (IEK-1), Forschungszentrum Jülich GmbH, 52425 Jülich, Germany

<sup>2</sup> Heinz Maier-Leibnitz Zentrum, TU München, 85747 Garching, Germany

<sup>3</sup> Deutsches Elektronen-Synchrotron (DESY), Notkestraße 85, 22607 Hamburg, Germany

<sup>4</sup> Institute of Crystallography, RWTH Aachen University, 52066 Aachen, Germany

\* Correspondence: y.sohn@fz-juelich.de

**Abstract:** Complex perovskite  $\text{La}_2(\text{Al}_{1/2}\text{MgTa}_{1/2})\text{O}_6$  (LAMT) crystallizes in a monoclinic unit cell with space group  $P2_1/n$  at room temperature. Its *B*-site cations are ordered in a rock-salt-type arrangement. Previously, the full occupancy of Mg on the  $2c$ -Wyckoff position was deduced from powder X-ray diffraction (PXRD). However, conventional X-rays could not properly resolve the mixed occupation on the *B*-site, since there is little scattering contrast between the neighbouring elements Mg and Al of the periodic table. Hence, complementary neutron diffraction studies were carried out to verify the exact *B*-site cation ordering in the unit cell. In this specific configuration of the *B*-cations, with its occupancy ratio and the presence of a heavy element Ta as well as neighbouring elements Mg and Al, only the strategy of a combined Rietveld analysis using both the X-ray and neutron diffraction data simultaneously succeeded in elucidating an accurate *B*-site cation ordering in this complex perovskite system. A full occupancy of Mg on the  $2c$ -Wyckoff position and each a half occupancy of Al and Ta on the  $2d$ -Wyckoff position could be resolved for the rock-salt-type ordering of the *B*-site cations in the monoclinic unit cell of LAMT.

**Keywords:** complex rare-earth perovskite; X-ray powder diffraction; neutron powder diffraction; combined Rietveld analysis; *B*-site cation ordering



**Citation:** Sohn, Y.J.; Baran, V.; Gilles, R.; Roth, G.; Vaßen, R. Combined X-ray and Neutron Powder Diffraction Study on *B*-Site Cation Ordering in Complex Perovskite  $\text{La}_2(\text{Al}_{1/2}\text{MgTa}_{1/2})\text{O}_6$ . *Solids* **2023**, *4*, 87–93. <https://doi.org/10.3390/solids4010006>

Academic Editor: Timothy J. Prior

Received: 16 January 2023

Revised: 6 February 2023

Accepted: 20 February 2023

Published: 1 March 2023



**Copyright:** © 2023 by the authors. Licensee MDPI, Basel, Switzerland. This article is an open access article distributed under the terms and conditions of the Creative Commons Attribution (CC BY) license (<https://creativecommons.org/licenses/by/4.0/>).

## 1. Introduction

Complex rare-earth perovskites with the general formula  $A(B'B'')\text{O}_3$  are among the promising candidates for thermal barrier coating (TBC) materials due to their high melting points as well as their high thermal expansion coefficient values [1–3]. Great efforts are made to increase gas turbine engine efficiency, for which higher inlet temperature is inevitable. In addition, a higher operation temperature leads to less  $\text{CO}_2$  production. Therefore, different approaches to find new materials [4,5], engineer high-performance coatings by designing more stable microstructures, or optimize operating conditions are suggested [1,5,6]. Recently, a considerably prolonged thermal cycling lifetime was reported using a complex perovskite as a TBC topcoat [5]. When  $\text{La}_2(\text{Al}_{1/2}\text{MgTa}_{1/2})\text{O}_6$  (LAMT) was applied through the suspension plasma spraying technique on the top of the state-of-the-art yttria partially stabilized zirconia (YSZ) layer, a highly porous columnar microstructure was achieved, allowing increased strain tolerance against thermally induced stress in the coating [5]. Notably, this kind of complex perovskite used as topcoats remained intact during thermal loading tests, and the failure of this system only occurred with the interface of the bondcoat (BC) and TBC layer [5]. These interesting material characteristics initiated further investigation on their crystal structure and phase transition behaviour at high temperatures [7].

An extensive crystal structure analysis through Rietveld refinements has been carried out at different temperatures via in situ high-temperature powder X-ray diffraction (PXRD) on LAMT powder [7]. However, an assumption has to be made regarding the Mg occupancy in the monoclinic unit cell at room temperature through Rietveld refinement, for there is little contrast between Mg and Al with X-rays. X-rays interact with electrons, and the scattering amplitude is proportional to their numbers. Moreover, the  $\text{Mg}^{2+}$  and  $\text{Al}^{3+}$  ions are isoelectronic, and have the same electronic configurations. Therefore, detecting the neighbouring elements of the periodic table, such as Mg and Al, precisely in a crystallographic unit cell is not possible via conventional X-ray diffraction. There is, though, a technique called X-ray anomalous diffraction, where the site occupancy of neighbouring elements can be resolved utilizing changes in anomalous dispersion factors  $f'$  and  $f''$  of each element near its absorption edges with varying incident X-ray wavelengths [8,9]. For our studies, a complementary neutron powder diffraction (NPD) method was chosen to properly characterize the B-site cation occupations. Neutrons interact directly with the nucleus of an atom and, together with other properties such as large beam cross section, deep penetration depth or no decrease in scattering intensity for high-scattering angles  $2\theta$ , they have shown to be very suitable for studies on high-temperature alloys [10,11]. Mg and Al have substantially different coherent scattering lengths (Mg: 5.375 fm, Al: 3.449 fm) for thermal neutrons [12], which now enables us to distinguish the Mg and Al atom positions in the unit cell. Since LAMT consists of a much heavier element, tantalum, on the B-site as well, a combined Rietveld refinement using both the PXRD and NPD data simultaneously was performed. This work aims to resolve the uncertainty in the B-site cation ordering in complex perovskite using PXRD and NPD techniques in a single, combined Rietveld refinement.

## 2. Materials and Methods

LAMT powder was prepared from stoichiometric amounts of  $\text{La}_2\text{O}_3$ ,  $\text{Al}_2\text{O}_3$ ,  $\text{MgO}$  and  $\text{Ta}_2\text{O}_5$  powders as described in earlier works [5,7]. A minor (5 wt%) secondary phase of  $\text{La}_3\text{TaO}_7$  was present in the investigated powder, but did not affect the crystal structure analysis of the main LAMT powder through Rietveld refinements.

PXRD was carried out using Empyrean (Malvern Panalytical, Almelo, The Netherlands) with  $\text{CuK}\alpha_{1,2}$  radiation at 45 kV and 40 mA. The PXRD data were collected in the  $2\theta$  range of  $10^\circ$  to  $150^\circ$  with  $\Delta 2\theta$  of  $0.013^\circ$  and a counting time of 500 s/step using a 255-channel PIXcel linear detector.

NPD was performed with the high-resolution powder diffractometer SPODI (FRM II, Garching, Germany) [11]. The powder was filled into a vanadium container with a diameter of 3 mm and a height of 20 mm. The NPD data were collected up to  $2\theta$  of  $152^\circ$  using a multidetector (80  $^3\text{He}$  position sensitive detector tubes) in a Debye Scherrer geometry using a wavelength of 1.54827 Å and a total data collecting time of 520 min. Silicon reference powder (NIST SRM 640c, NIST, Ceramic Division, Gaithersburg, MA, USA) was used for obtaining the instrumental resolution function in the same measurement setting.

Combined Rietveld analysis on PXRD and NPD data was conducted with the software TOPAS (Bruker AXS, Karlsruhe, Germany) [13].

## 3. Results and Discussion

### 3.1. Neutron Powder Diffraction Data Analysis

Si-reference powder data were collected in the same instrumental settings as for our LAMT powder to obtain the instrumental resolution function for the peak profiles. Using the TOPAS software, the Chebyshev polynomial with six coefficients was used for the background description, and the modified Thompson–Cox–Hastings pseudo-Voigt function with a peak asymmetry parameter was chosen for the peak profile. The Rietveld refinement result of the Si-reference powder resulted in the weighted R-value ( $R_{\text{wp}}$ ) of 4.75%. Those initial parameters of the peak profile function from the Si-reference data were then fixed and only the domain size and the microstrain parameters were refined

for the LAMT NPD data. The first attempts of refining the NPD data alone did not result in unambiguous solutions of the Mg occupancy as expected. Although Mg and Al now have distinct contrast in their neutron scattering lengths, the sum of  $1/2$  Al +  $1/2$  Ta (Ta: 6.91 fm [12]) being 5.180 fm almost equals the full occupancy of Mg with 5.375 fm. Therefore, different structural models resulted in similar  $R_{wp}$  factors. At this point, the X-ray powder diffraction data should be beneficial, because the much heavier element tantalum, as one of the *B*-site cations, should be easily distinguishable from the weak scatterers Mg and Al.

### 3.2. Ta Detection in the Unit Cell through X-rays

Through chemical analysis, we are certain that the ratio of the *B*-site cations should be Mg:Al:Ta = 1:0.5:0.5. Additionally, we assume a full occupancy of two symmetry equivalent positions for the *B*-site cations in the monoclinic unit cell. With these constraints, the two possible Wyckoff positions,  $2c$  and  $2d$ , were refined freely. The converged Rietveld refinement detected the heavy element Ta on the  $2d$ -Wyckoff position with a refined occupancy of 0.518(1). Ta now having been successfully localized on the  $2d$ -Wyckoff position through PXRD data, two different crystal structure models of the space group symmetry  $P2_1/n$  (No. 14 [14]) were chosen, regarding the Mg occupancy of LAMT at room temperature: (1) full occupancy of Mg on the  $2c$ -Wyckoff position, and  $1/2$  Al +  $1/2$  Ta on the  $2d$ -Wyckoff position and (2)  $1/2$  Mg +  $1/2$  Al on the  $2c$ -Wyckoff position, and  $1/2$  Mg +  $1/2$  Ta on the  $2d$ -Wyckoff position. In the case of PXRD data, these two models are not distinguishable due to the little contrast between Mg and Al. Hence, the combined Rietveld refinement on both the PXRD and NPD data simultaneously was conducted.

### 3.3. Combined Rietveld Analysis on X-ray and Neutron Powder Diffraction Data

The data sets from X-ray and neutron experiments were obtained on the same LAMT powder at room temperature and were used simultaneously in a combined Rietveld analysis. The background parameters, the lattice parameters, the sample displacement parameters and the peak profile parameters were refined separately for each data set. For the PXRD data, a fundamental parameters approach [15] implemented in the software TOPAS was utilized to describe the peak profiles, which takes the instrumental settings into account. The broadening of the peak profiles, in this case, can then be ascribed to the microstructural effects of the sample, i.e., domain size and microstrain. Now, a more accurate crystal structure model refinement can be carried out involving the two data sets simultaneously, but refining the atomic parameters jointly. Returning to our crystal structure models described in Section 3.2., the NPD data responded sensitively to the *B*-site cation ordering due to the significantly different scattering lengths of Mg and Al. A notable discrepancy between the observed and the calculated Bragg peak intensities was now detectable for each structure model, as shown in Figure 1a. The (011)-Bragg peak chosen here as an example represents a lattice plane in the monoclinic  $P2_1/n$  unit cell where the *B*-site cations are aligned (Figure 1b). The  $R_{wp}$  of the two structure models are  $R_{wp} = 4.33\%$  for the full Mg occupancy and  $R_{wp} = 4.43\%$  for the half Mg occupancy, respectively.

Observed ( $Y_{obs}$ ), calculated ( $Y_{calc}$ ) and difference ( $Y_{obs} - Y_{calc}$ ) powder diffraction patterns of the combined Rietveld refinements are shown in Figure 2a,b for X-ray and neutron experiments, respectively. A minor secondary phase of  $La_3TaO_7$  (space group symmetry,  $Cmcm$ ) was present in the powder, and quantified to 5 wt % through Rietveld analysis.

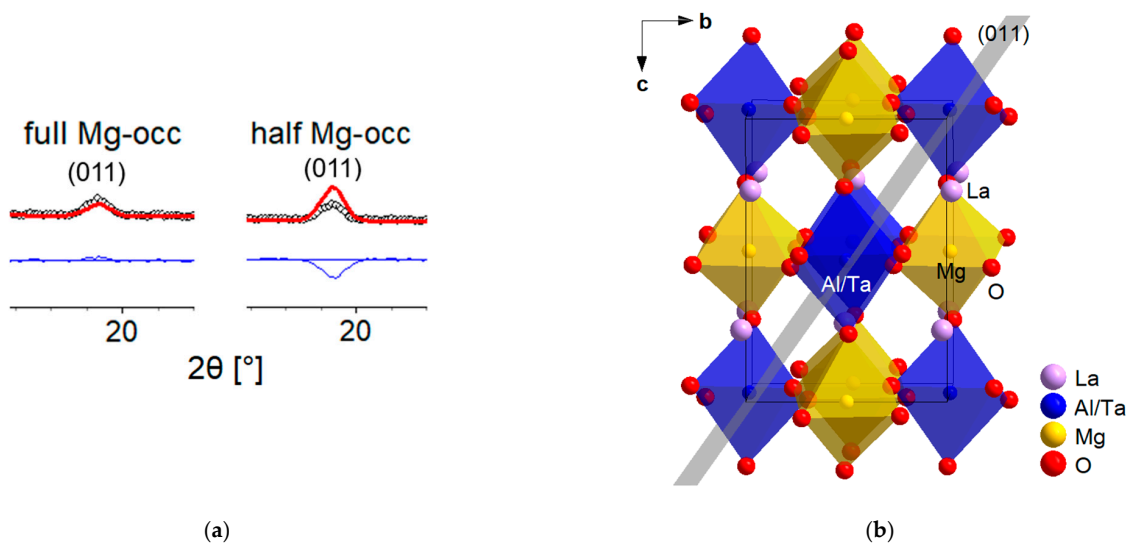


**Figure 1.** Mg occupancy of LAMT: (a) Discrepancy of the (011)-Bragg peak intensity on the NPD data between the full and half Mg occupancy; (b) (011)-plane in the monoclinic unit cell. Isotropic displacement parameters are visualized at the 50% probability level.

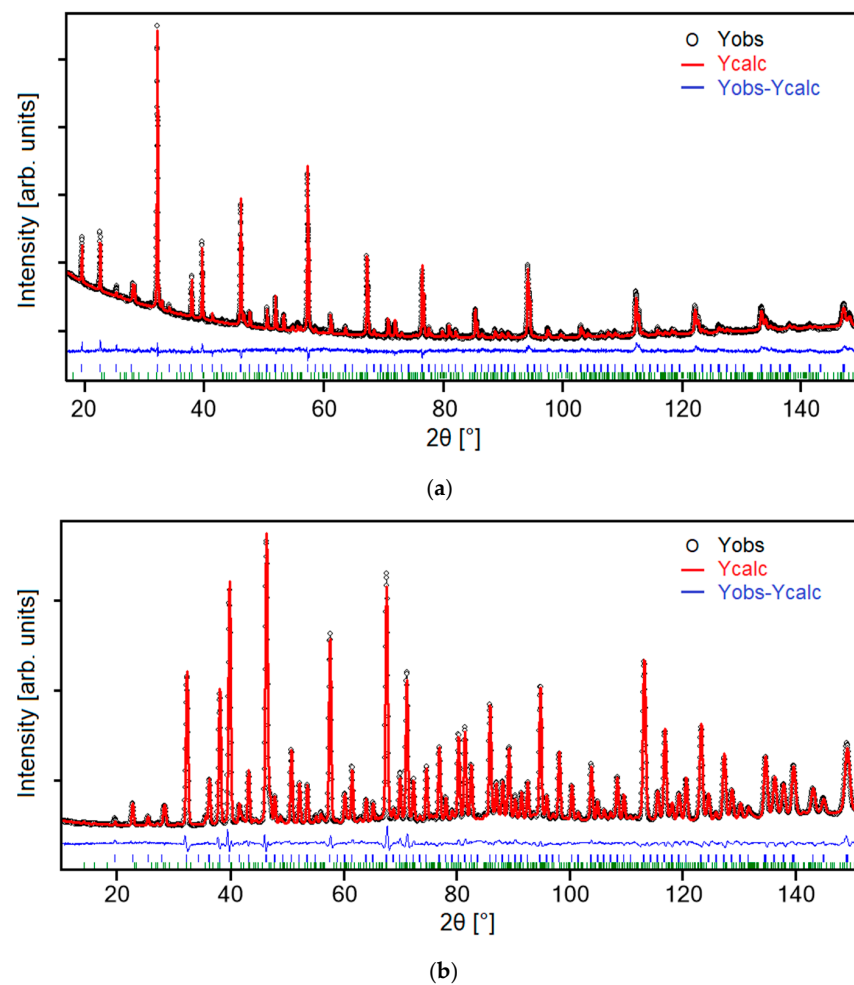


**Figure 2.** Combined Rietveld refinement of (a) PXRD data; (b) NPD data. Bragg peak positions are indicated as vertical lines below the difference curve, LAMT in blue,  $\text{La}_3\text{TaO}_7$  in green.

The results of the combined Rietveld analysis are summarized in Table 1. The atomic displacement parameters of all oxygen atoms were constrained to the same isotropic value ( $B_{\text{iso}}$ ) due to no meaningful values coming out of an anisotropic refinement. Crystallographic Information Files (CIFs) of the Si-reference (S1) and the LAMT (S2) have been deposited in the supplementary materials.

**Table 1.** Results of combined Rietveld analysis on LAMT.

	X-ray	Neutron
Crystal system, Space group	Monoclinic, $P2_1/n$	
Lattice parameters: $a, b, c$ [Å], $\beta$ [°]	5.566 (6)	5.567 (2)
	5.568 (9)	5.565 (2)
	7.867 (6)	7.866 (2)
	89.98 (30)	89.97 (9)
Unit cell volume [Å <sup>3</sup> ]	243.78 (60)	243.73 (15)
Atomic parameters [Wyckoff position, $x, y, z$ , Occ., $B_{\text{iso}}$ ]		
La	4e, 0.4932 (2), 0.4764 (1), 0.2456 (5), 1, 1.566 (13)	
Al/Ta	2d, 0.5, 0, 0, 0.5, 0.663 (8)	
Mg	2c, 0, 0.5, 0, 1, 0.663 (8)	
O1	4e, 0.2274 (6), 0.2197 (7), 0.0335 (3), 1, 1.072 (8)	
O2	4e, 0.2854 (5), 0.7206 (7), 0.0396 (3), 1, 1.072 (8)	
O3	4e, 0.5734 (2), 0.0123 (2), 0.2489 (8), 1, 1.072 (8)	
$R_{\text{Bragg}}$	3.66	2.67
$\chi^2, R_{\text{wp}}, R_{\text{p}}$	3.71, 4.33, 3.22	
Domain size and microstrain [ $D_{\text{v}}, e$ ]	>200 nm, $2.9 (1) \cdot 10^{-4}$	

Note: Occ. = site occupancy factor,  $B_{\text{iso}}$  = isotropic atomic displacement parameter in Å<sup>2</sup>,  $R_{\text{Bragg}} = \sum |I_{\text{o}} - I_{\text{c}}| / \sum I_{\text{o}}$ ,  $\chi^2 = (\sum w (Y_{\text{o}} - Y_{\text{c}})^2 / M - P)^{1/2}$ ,  $R_{\text{wp}} = (\sum w (Y_{\text{o}} - Y_{\text{c}})^2 / \sum w Y_{\text{o}}^2)^{1/2}$ ,  $R_{\text{p}} = \sum |Y_{\text{o}} - Y_{\text{c}}| / \sum Y_{\text{o}}$  where  $I_{\text{o}}$ : observed intensity,  $I_{\text{c}}$ : calculated intensity,  $w = 1/\sigma (Y_{\text{o}})^2$ ,  $Y_{\text{o}}$ : observed data,  $Y_{\text{c}}$ : calculated data,  $M$ : number of data points,  $P$ : number of parameters,  $D_{\text{v}}$  = volume-weighted domain size as described in [16],  $e$  = strain as described in [17].

Selected interatomic distances and bond angles are provided in Table 2. These values correspond well with the literature values of similar complex rare-earth perovskites,  $\text{La}_2\text{Mg}(\text{Mg}_{1/3}\text{Ta}_{2/3})\text{O}_6$  [18] and  $\text{La}(\text{Mg}_{2/3}\text{Nb}_{1/3})\text{O}_3$  [19], where the B-site cations are also arranged in a rock-salt-type ordering. The mean distances of the Al/Ta-O (1.984 Å) and Mg-O (2.025 Å) of LAMT are also in good agreements with the calculated values (1.99 Å for Ta-O; 2.07 Å for Mg-O) using the ionic radii by Shannon [20].

**Table 2.** Selected interatomic distances and angles of LAMT.

La-O [Å]	2.410 (4) – 3.292 (4)
<La-O>	2.799
Al/Ta-O [Å]	1.966 (4) × 2 1.985 (3) × 2 2.001 (6) × 2
<Al/Ta-O>	1.984
Mg-O [Å]	2.018 (6) × 2 2.026 (4) × 2 2.032 (3) × 2
<Mg-O>	2.025

Table 2. Cont.

Al/Ta-O-Mg [°]	156.2 (3)
	160.6 (2)
	156.9 (2)
O-Al/Ta-O [°]	90.2 (1) × 2
	89.7 (1) × 2
	89.8 (1) × 2
	90.3 (1) × 2
	89.9 (1) × 2
	90.1 (1) × 2
O-Mg-O [°]	87.5 (1) × 2
	92.5 (1) × 2
	91.4 (1) × 2
	89.3 (1) × 2
	88.6 (1) × 2
	90.7 (1) × 2

This kind of combined Rietveld analysis benefits from the strengths of each scattering technique, in our case, the better detection of heavy elements via X-ray diffraction and high sensitivity of neighbouring elements in the periodic table via neutron diffraction.

#### 4. Conclusions

Complementary powder diffraction techniques using X-ray and neutron sources and combining these data in a simultaneous Rietveld refinement yielded a more accurate crystal structure analysis on LAMT. A thorough investigation of the heterogeneous *B*-site cation ordering of Mg, Al and Ta was established involving both of the techniques. The heavy element Ta could well be detected through X-rays, whereas the neighbouring elements Mg and Al, with their different characteristic scattering lengths, through neutrons revealed their exact configuration in the crystal structure. Hence, a full occupancy of Mg on the 2*c*-Wyckoff position and each a half occupancy of Al and Ta on the 2*d*-Wyckoff position could be pinned down in the end.

**Supplementary Materials:** Crystallographic Information Files (CIFs) can be downloaded at: <https://www.mdpi.com/article/10.3390/solids4010006/s1>, Supplementary S1: Si-reference.cif; Supplementary S2: LAMT.cif.

**Author Contributions:** Conceptualization, Y.J.S.; methodology, Y.J.S. and V.B.; formal analysis, Y.J.S.; investigation, Y.J.S. and V.B.; writing—original draft preparation, Y.J.S.; writing—review and editing, V.B., R.G., G.R. and R.V. All authors have read and agreed to the published version of the manuscript.

**Funding:** This research received no external funding.

**Data Availability Statement:** Not applicable.

**Acknowledgments:** The authors thank Michaela Andreas for the powder sample. FRM II (Garching, Germany) is also gratefully acknowledged for granted beamtime at SPODI within the Rapid Access Program. We sincerely thank the anonymous reviewers for their helpful comments on this work.

**Conflicts of Interest:** The authors declare no conflict of interest.

#### References

1. Vaßen, R.; Jarligo, M.O.; Steinke, T.; Mack, D.E.; Stöver, D. Overview on advanced thermal barrier coatings. *Surf. Coat. Technol.* **2010**, *205*, 938–942. [CrossRef]
2. Guo, R.; Bhalla, A.S.; Cross, L.E. Ba(Mg<sub>1/3</sub>Ta<sub>2/3</sub>)O<sub>3</sub> single crystal fiber grown by the laser heated pedestal growth technique. *J. Appl. Phys.* **1994**, *75*, 4704–4708. [CrossRef]
3. Jarligo, M.O.; Mack, D.E.; Vassen, R.; Stöver, D. Application of plasma-sprayed complex perovskites as thermal barrier coatings. *J. Therm. Spray Technol.* **2009**, *18*, 187–193. [CrossRef]

4. Gilles, R.; Mukherji, D.; Karge, L.; Strunz, P.; Beran, P.; Barbier, B.; Kriele, A.; Hofmann, M.; Eckerlebe, H.; Rösler, J. Stability of TaC precipitates in a Co-Re-based alloy being developed for ultra-high-temperature applications. *J. Appl. Cryst.* **2016**, *49*, 1253–1265. [[CrossRef](#)]
5. Schlegel, N.; Sebold, D.; Sohn, Y.J.; Mauer, G.; Vaßen, R. Cycling performance of a columnar-structured complex perovskite in a temperature gradient test. *J. Therm. Spray Technol.* **2015**, *24*, 1205–1212. [[CrossRef](#)]
6. Vaßen, R.; Mack, D.E.; Tandler, M.; Sohn, Y.J.; Sebold, D.; Guillon, O. Unique performance of thermal barrier coatings made of yttria-stabilized zirconia at extreme temperatures (>1500 °C). *J. Am. Ceram. Soc.* **2021**, *104*, 463–471. [[CrossRef](#)]
7. Sohn, Y.J.; Mauer, G.; Roth, G.; Guillon, O.; Vaßen, R. Crystal structure analysis and high-temperature phase transitions of complex rare-earth perovskite,  $\text{La}_2(\text{Al}_{1/2}\text{MgTa}_{1/2})\text{O}_6$ . *J. Am. Ceram. Soc.* **2020**, *103*, 1404–1413. [[CrossRef](#)]
8. Smaha, R.W.; Boukahil, I.; Titus, C.J.; Jiang, J.M.; Sheckelton, J.P.; He, W.; Wen, J.; Vinson, J.; Wang, S.G.; Chen, Y.S.; et al. Site-specific structure at multiple length scales in kagome quantum spin liquid candidates. *Phys. Rev. Mater.* **2020**, *4*, 1–12. [[CrossRef](#)] [[PubMed](#)]
9. Freedman, D.E.; Han, T.H.; Prodi, A.; Müller, P.; Huang, Q.Z.; Chen, Y.S.; Webb, S.M.; Lee, Y.S.; McQueen, T.M.; Nocera, D.G. Site specific X-ray anomalous dispersion of the geometrically frustrated kagomé magnet, herbertsmithite,  $\text{ZnCu}_3(\text{OH})_6\text{Cl}_2$ . *J. Am. Chem. Soc.* **2010**, *132*, 16185–16190. [[CrossRef](#)] [[PubMed](#)]
10. Gilles, R. How neutrons facilitate research into gas turbines and batteries from development to engineering applications. *J. Surf. Investig.* **2020**, *14* (Suppl. 1), S69–S74. [[CrossRef](#)]
11. Hoelzel, M.; Senyshyn, A.; Juenke, N.; Boysen, H.; Schmahl, W.; Fuess, H. High-resolution neutron powder diffractometer SPODI at research reactor FRM II. *Nucl. Instrum. Methods Phys. Res. A* **2012**, *667*, 32–37. [[CrossRef](#)]
12. Prince, E. *International Tables for Crystallography Volume C: Mathematical, Physical and Chemical Tables*, 3rd ed.; Wiley: Chichester, UK, 2006; pp. 444–454.
13. *TOPAS V4: General Profile and Structure Analysis Software for Powder Diffraction Data*; Bruker AXS: Karlsruhe, Germany, 2008.
14. Aroyo, M.I. *International Tables for Crystallography Volume A: Space-Group Symmetry*; Kluwer Academic Publishers: Dordrecht, The Netherlands, 2016.
15. Cheary, R.W.; Coelho, A. A fundamental parameters approach to X-ray line-profile fitting. *J. Appl. Cryst.* **1992**, *25*, 109–121. [[CrossRef](#)]
16. Balzar, D.; Audebrand, N.; Daymond, M.R.; Fitch, A.; Hewat, A.; Langford, J.I.; Le Bail, A.; Louër, D.; Masson, O.; McCowan, C.N.; et al. Size-strain line-broadening analysis of the ceria round-robin sample. *J. Appl. Cryst.* **2004**, *37*, 911–924. [[CrossRef](#)]
17. Balzar, D. Voigt function model in diffraction-line broadening analysis. In *Defect and Microstructure Analysis by Diffraction*; Snyder, R.L., Fiala, J., Bunge, H.J., Eds.; International Union of Crystallography, Oxford University Press Inc.: New York, NY, USA, 1999; pp. 94–124.
18. Kim, Y.I.; Woodward, P.M. Crystal structures and dielectric properties of ordered double perovskites containing  $\text{Mg}^{2+}$  and  $\text{Ta}^{5+}$ . *J. Solid State Chem.* **2007**, *180*, 2798–2807. [[CrossRef](#)]
19. Choi, I.K.; Cho, B.J.; Paik, J.H.; Nahm, S.; Kim, J.S.; Lee, H.J.; Park, H.M.; Byun, J.D.; Ahn, B.G. Crystal structure of  $\text{La}(\text{Mg}_{2/3}\text{Nb}_{1/3})\text{O}_3$  ceramics. *Mater. Res. Bull.* **2000**, *35*, 921–928. [[CrossRef](#)]
20. Shannon, R.D. Revised effective ionic radii and systematic studies of interatomic distances in halides and chalcogenides. *Acta Cryst. A* **1976**, *32*, 751–767. [[CrossRef](#)]

**Disclaimer/Publisher’s Note:** The statements, opinions and data contained in all publications are solely those of the individual author(s) and contributor(s) and not of MDPI and/or the editor(s). MDPI and/or the editor(s) disclaim responsibility for any injury to people or property resulting from any ideas, methods, instructions or products referred to in the content.